Ocean Engineering 38 (2011) 1065–1079

Contents lists available at ScienceDirect

Ocean Engineering

journal homepage: www.elsevier.com/locate/oceaneng

# CFD simulations of the effects of fouling and antifouling

Yee Shin Khor, Qing Xiao *

*University of Strathclyde, Glasgow G4 0LZ, UK*

ARTICLE INFO

*Article history:*
Received 30 November 2010
Accepted 19 March 2011
Editor-in-Chief: A.I. Incecik
Available online 7 May 2011

*Keywords:*
Fouling and antifouling
Lift–drag ratio
Computational fluid dynamics

ABSTRACT

Biofouling is a global problem in the marine industry though its effects on lift and drag are rarely discussed. This paper seeks to employ Computational Fluid Dynamics (CFD) method to quantify the effects of this problem based on the obtained flow field information. The simulation is carried out on a NACA 4424 airfoil and Defence Research Establishment Atlantic (DREA) Submarine Hull. Different levels of fouling are studied with quantified fouling height and density. As an extension, the effects of two common antifouling methods, i.e. tin-free Self-Polishing Copolymer (SPC) and Foul Release on the drag of NACA 4424 foil and the submarine hull is investigated. For NACA 4424 airfoil, fouling reduces lift–drag ratio ($C_L/C_D$) by up to 80% in maximum and therefore result in the significant increase in fuel consumption. Predicted flow data shows this is related to the increased flow separation region caused by the fouling. It is found that pressure gradient gradually increases from the smallest fouling height to the largest but does not vary that much for fouling of varying densities. The general trend of $C_L/C_D$ varies with angle of attack agrees well with others experimental data. Computed results also show good agreement with experimental data for the DREA bare hull. As to antifouling, Foul Release, despite being 30% more expensive than SPC, exhibits 10–40% higher $C_L/C_D$ as compared to SPC for NACA foil and submarine hull.



## 1. Introduction

Fouling is defined as 'undesired deposition of material on surfaces' while biofouling is defined as 'deposition and growth of microorganisms on surfaces' (Epstein, 1981). Biofouling has three main negative effects which include increase in drag and hence resistance and fuel consumption, damages to underlying paint films and transfer of invasive aquatic species (Drake and Lodge, 2007; Woods Hole Oceanographic Institute, 1952; Wood and Allen, 1958). Microscopic and macroscopic are two groups of fouling organisms. Previous studies (Woods Hole Oceanographic Institute, 1952; Wood and Allen, 1958) showed that effects of microscopic organisms are considerably less damaging as compared to macroscopic organisms. Of all the macroscopic organisms, barnacles from the arthropods group receive the widest attention as they are usually found on the ship bottom (Woods Hole Oceanographic Institute, 1952). This is reaffirmed in reports which listed *Balanus Amphitrite* (a species of barnacles) as the most common fouling organism in Australian waters, eastern Indian waters and Lake Timsah, the most heavily fouled area in Egypt, respectively (Rajagopal et al., 1997; Ghobashy and El Komy, 1980; Hentschel, 1923). Barnacles also top the list in Hamburg waters and US waters (Visscher, 1927; Anderson, 2006). This is due to barnacles' characteristics such as having quick growth rate, indiscriminate choice of underlying support and being hermaphroditic (Woods Hole Oceanographic Institute, 1952). Therefore, barnacles can be a good model for fouling research.

Towards the end of the 20th century, antifouling takes a biocidal approach. Fungicide TBTO (tributyltin oxide) is easily handled and compatible with many other biologically active compounds leading to high efficiency. However, tributyltin (TBT)'s toxicity to other marine organisms, rate of degradation and potential for bio-accumulation became a major concern (Anderson, 2006). International Maritime Organisation (IMO) has banned all application of TBT-based coatings by 1 January 2003 and all remaining use of TBT-based coatings by 1 January 2008. Although this has taken the shipping industry by surprise, new solutions quickly appeared. Currently, all antifouling release mechanism can be divided into TBT-free biocidal solutions and foul release coating. For TBT-free biocidal solutions, there is Self-Polishing Copolymer (SPC), Controlled Depletion Polymer (CDP) or hybrid SPC (Anderson, 2006). However, International Towing Tank Conference (ITTC) stated in its 2005 report that there is no accurate method to measure the effect of ship roughness from the use of antifouling paints (ITTC, 2005).

Investigation of hull biofouling and antifouling has not met much effort despite their significant effects on ships' operation costs.

* Corresponding author. Tel.: +44 141 5484779; fax: +44 141 5522879
*E-mail addresses:* yee.khor@strath.ac.uk, qing.xiao@strath.ac.uk (Q. Xiao).

0029-8018/$ - see front matter © 2011 Elsevier Ltd. All rights reserved.
doi:10.1016/j.oceaneng.2011.03.004

**Nomenclature**

| | |
|---|---|
| $\alpha$ | angle of attack in degrees |
| $c$ | chord length of foil |
| $C_D$ | drag coefficient |
| $C_L$ | lift coefficient |
| $h$ | antifouling roughness parameter |
| $Re$ | Reynolds number, $Re=U_\infty c/\upsilon$ |
| $U_\infty$ | free-stream velocity. |
| $\nu$ | fluid viscosity |

Orme et al. (2001) studied the fouling effects on a NACA 4424 airfoil in a wind tunnel experiment, by applying extruded small conical shapes to model barnacles fouling. Resemblance to real situation is enhanced by sample collection beforehand to increase understanding of the barnacles fouling community. Results are in the form of airfoil's lift coefficient and drag coefficient $C_L$ and $C_D$, which can be applied directly to other practical uses such as resistance on a ship's hull. As expected, drag was found to increase when fouling occurred but stall angle increased by 10° with fouling. The maximum $C_L/C_D$ ratio was found to be at least 70% lower with the presence of fouling. Although some information has been provided on the fouling effect, it lacks the precision because no detailed flow visualisation could be offered.

In Candries and Atlar (2003), the effect of antifouling on flat plate and cylinder was examined by experimental roughness tests. Efforts were made to link the roughness to drag and hence resistance. Two of the popular types of antifouling, i.e. tin-free Self Polishing Copolymer (SPC) and Foul Release were applied on flat plates (for experiments in water tunnel or towing tank) or cylinder (rotor experiment) and their corresponding roughness profiles were recorded. All measurements were produced by the BMT Hull Roughness Analyser. Results showed that tin-free SPC exhibits more drag as compared to Foul Release due to larger roughness. However, the average hull roughness (AHR) values did not correlate with the drag values. For example, in a 6.3 m long flat plate experiment, the AHRs for SPC and Foul Release are 39 and 62 μm, respectively, but drag value is higher for SPC. They suggested that AHR is therefore not the best parameter for roughness in drag calculations. Instead, a better parameter was suggested, $h$ derived from the Colebrook–White function. The value $h$ is defined as follows:

$$h = R_a \Delta a/2 \tag{1}$$

where $R_a$ is centreline average roughness height and $\Delta a$ is mean absolute slope. The $h$ value in metres can be obtained experimentally and forms a direct relationship with drag.

In the papers above, it appears that while fouling and antifouling effects on lift and drag have seen research efforts, a systematic investigation of their effects on flow structure is not yet available due to limitations of experimental methods. The aim of the present study is therefore to fill this gap by utilising Computational Fluid Dynamics (CFD) method.

CFD is the art of replacing the integrals or the partial derivatives of fundamental physical principles in mathematical equations with discretized algebraic forms (Anderson, 1995). The governing equations are basic physical principles of mass, momentum and energy conservation. Its use in marine research has been gaining strength and some research on antifouling has been done using CFD. Ndinisa et al. (2006) investigates the effectiveness of gas–liquid two-phase flow as a method of antifouling for a submerged flat plate membrane system which provides a direct relationship between fouling and resistance.

The objective of this study is to investigate the flow effects of fouling and antifouling on the lift and drag forces of marine devices with relative simple geometries. Two typical shapes are selected, e.g. NACA 4424 airfoil and DREA (Defence Research Establishment Atlantic) Submarine Hull (Baker, 2004). The later geometry is specifically chosen because it is a standard submarine design due to its simple outer geometry. Different from previous studies, despite the overall lift and drag force investigation, we will concentrate more on the fouling/antifouling effect on the flow details such as flow separation, surface pressure distribution and turbulent kinetic energy distribution which are believed to shed more insight on the flow mechanism, and thus provide more useful information for industrial design. In addition, the relevance of computed results to the marine engineering will be fully discussed.

In the following, the numerical details will be described in Section 2 followed by the results and discussions in Section 3. Conclusions will be drawn at the end.

## 2. Numerical approach

### 2.1. Geometry of bare airfoil and DREA submarine hull and relevant parameters

Geometry of bare NACA 4424 airfoil is shown in Fig. 1. The general geometrical formulae for DREA submarine hull are as follows: The 2-D axisymmetric hull form of DREA submarine with a maximum length, $l$ and diameter, $d$ can be divided into three regions of geometry, i.e., nose, central body and tail. The radius of the DREA hull in each of these regions is defined as $r_1$, $r_2$ and $r_3$, respectively, as shown in Fig. 2. They can be calculated using the equations of geometry below. As can be seen, they are functions of $x$, which is the centreline distance from the nose tip.

$$\frac{r_1(x)}{l} = \frac{d}{l}\left[2.56905\sqrt{x - 3.48055x + 0.49848(x)^2 + 3.40732(x)^3}\right] \quad \text{for } 0 \le x \le 0.2 \tag{2}$$

$$\frac{r_2(x)}{l} = \frac{d}{2l} \quad \text{for } 0.2 \le x \le 1 - \frac{3d}{l} \tag{3}$$

$$\frac{r_3(x)}{l} = \frac{d}{2l} - \frac{l}{18d}\left[x - \left(1 - \frac{3d}{l}\right)\right]^2 \quad \text{for } 1 - \frac{3d}{l} \le x \le 1 \tag{4}$$

The detailed geometric parameters of DREA submarine modelling in the present study include the length from tip to tail of 6.0 m, maximum half-breath of 0.343 m and length–breath ratio of 8.75 as shown in Fig. 2. Due to the symmetry, only top half of hull is displayed in Fig. 2.

### 2.2. Fouling and antifouling modelling

#### 2.2.1. Fouling

Fouling is modelled by setting small conical shapes on the surface of airfoil as proposed in the experimental study of Orme et al. (2001). For a two-dimensional foil examined here, it is simplified by using the spikes resembling fouling as shown in Fig. 3.

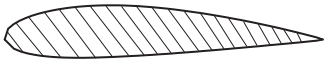

**Fig. 1.** NACA 4424 Airfoil.

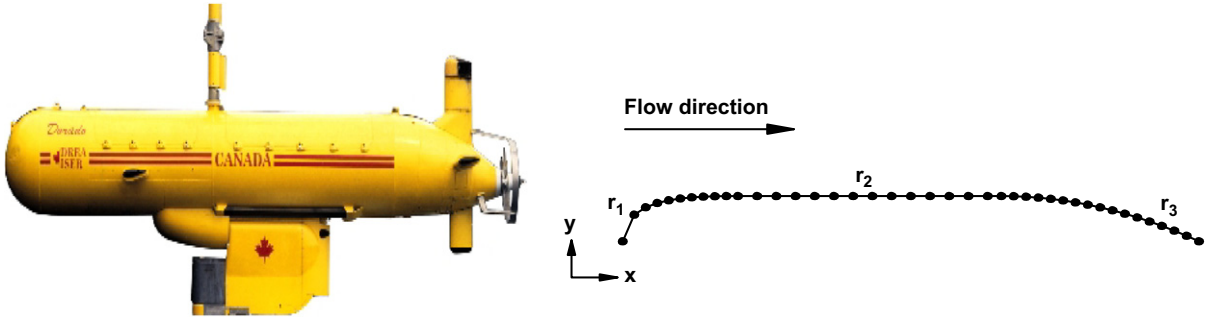


**Fig. 2.** Experimental model from Baker (2004) (left) and present computational model (right) of DREA submarine hull.

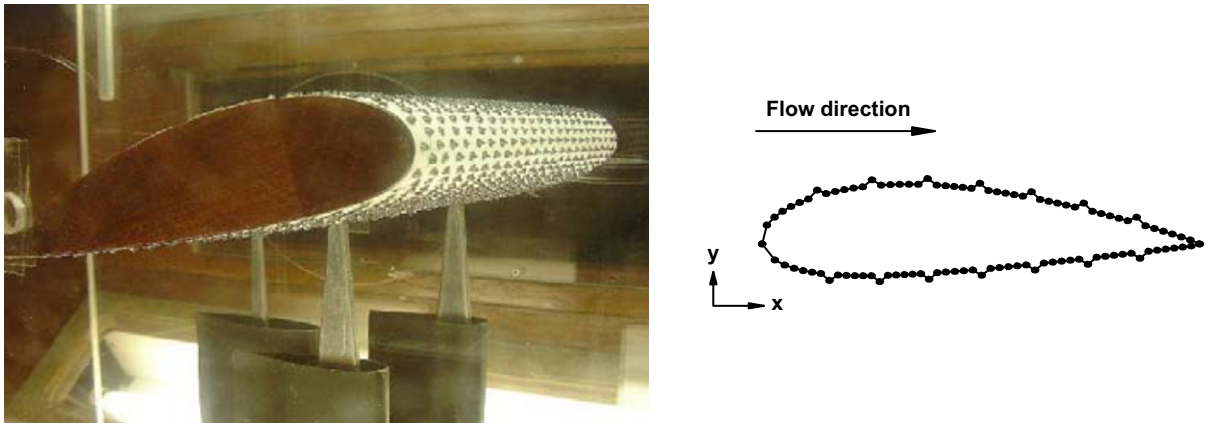


**Fig. 3.** Experimental model from Orme et al. (2001) (left) and present computational model (right) of NACA 4424 Airfoil.

**Table 1**
Experimental fouling cases (from Orme et al., 2001).

| Variable | Height *h* | Density *f* |
|---|---|---|
| | Model barnacle height m | Model barnacles per $m^2$ |
| Paper only (control) | 0 | 0 |
| Small | 0.0007 | 21,389 |
| Medium | 0.0032 | 21,389 |
| Large | 0.0057 | 21,389 |
| Wide mesh | 0.0032 | 11,389 |
| Medium mesh | 0.0032 | 21,389 |
| Fine mesh | 0.0032 | 42,253 |

**Table 2**
Computational fouling cases.

| Case | Height (m) | Spacing (points) | Total spikes on each side |
|---|---|---|---|
| **NoFoul** | 0.0000 | N/A | 0 |
| **MinHe_MedSp** | 0.0007 | 5 | 7 |
| **MedHe_MedSp** | 0.0032 | 5 | 7 |
| **MaxHe_MedSp** | 0.0057 | 5 | 7 |
| **MedHe_MaxSp** | 0.0032 | 11 | 4 |
| **MedHe_MinSp** | 0.0032 | 2 | 15 |

**Table 3**
NACA 4424 details.

| | |
|---|---|
| Maximum length of camber, *m* (m) | 0.04*c* |
| Thickness of airfoil, *t* (m) | 0.24*c* |
| Position of camber from leading edge, *p* (m) | 0.40*c* |
| Fouling heights (m) | 0.0007, 0.0032, 0.0057 |
| Spacing between fouled points | 2, 5, 11 |
| Chord length (m) | 0.2 |

The experimental setting is summarised in Table 1. As seen, fouling cases are divided into two categories: height and density. Fouling height can be defined as the maximum length between the original airfoil surface and each individual spike (which represents the fouling organism). Fouling density is defined as the centre-to-centre length between two neighbouring spikes. To investigate the effects of fouling height alone, density was set to be constant and moderate (the same density with a medium mesh). To investigate the effects of fouling density, size was also made constant at medium height. Furthermore, a control case (in which the airfoil is wrapped in a blank piece of paper) was also set up alongside a smooth airfoil case for comparison purposes.

In computational modelling, the paper control case is not necessary as the 'fouling spikes' are not attached onto a piece of paper. Coordinates of the airfoil profile can be modified to fit in the 'spikes' which resemble fouling.

Distribution of fouling is much harder to model. Spacing between each conical shape was not given in the experimental setting; instead density in 3D was given. There are 51 points on each side of the airfoil so spacing between spikes can be estimated in a way that the spacing is constant and spacing is lesser for worse fouling cases. Spikes are not fitted at the trailing and leading edges to avoid adverse near-wall conditions.

With these thoughts in mind, the following fouling cases in Table 2 can now be set up. Different fouling height effect of MinHe_MedSp, MedHe_MedSp and MaxHe_MedSp is examined at a fixed fouling spacing. The effect of various fouling spacing is studied with a fixed fouling height of 0.0032 m. The summary of geometrical information and fouling details of NACA 4424 is given in Table 3.

#### 2.2.2. Antifouling

Antifouling, on the other hand is modelled by roughness height values as set out in Candries and Atlar (2003). A roughness unit $h$ is introduced and is defined in Eq. (1). However, the closest parameter in our CFD simulation package (FLUENT) for roughness modelling is equivalent sand-grain roughness $k_s$. A conversion from $h$ to $k_s$ is made on the following formula:

$$k_s = \frac{9.793}{C_s} h \tag{5}$$

where $C_s$ is the roughness constant (usually 0.5).

However, $k_s$ value also depends on length of model and $R_e$ of flow. This effect is explained using an equation by Townsin et al. (1984)

$$10^3 \Delta C_f = 44\left[\left(\frac{h}{L}\right)^{1/3} - 10R_e^{-1/3}\right] + 0.125 \tag{6}$$

Due to the complex nature of the equation, amplification factors are used instead. Final values of $k_s$ used are shown in Table 4.

### 2.3. Computational method

#### 2.3.1. Governing equations

The simulation is conducted by using a commercial Computational Fluid Dynamics package FLUENT. The general forms of the governing equations include the continuity equation, Navier–Stokes equations (momentum equations) as well as turbulence modelling equations which are summarised below:Continuity equation:

$$\frac{\partial}{\partial t}\int_V \rho\, dV + \oint_S \rho \boldsymbol{V}\cdot\boldsymbol{n}\, dS = 0 \tag{7}$$

where $V$ is volume, $\boldsymbol{V}$ is velocity vector, $\boldsymbol{n}$ is a normal vector and $dS$ is surface area integral. As flow is incompressible, density is assumed to be constant. The first term on the left disappears and continuity equation becomes:

$$\oint_S \boldsymbol{V}\cdot\boldsymbol{n}\, dS = 0 \tag{8}$$

Momentum conservation

$$\frac{\partial}{\partial t}\int_V \rho\boldsymbol{V}\, dV + \oint_S (\rho\boldsymbol{V})\boldsymbol{V}\cdot\boldsymbol{n}\, dS = \int_V \rho\boldsymbol{b}\, dV - \oint_S p\boldsymbol{n}\, dS + \oint_S \hat{T}\cdot\boldsymbol{n}\, dS \tag{9}$$

The Reynolds number based on the incoming velocity and chord length ($Re$) for flow around the airfoil is $4.8\times10^5$ and $2\times10^7$ for flow around the submarine hull. Therefore, both flows are considered as turbulent and turbulence models are required.

Standard $k$–$\varepsilon$ equation is a very popular two-equation turbulence model in the commercial software FLUENT. Due to its generally robust nature, it is widely used in industrial applications. It has advantage over other models in resolving free shear flows but has shown weakness in near-wall modelling because the turbulence equations cannot be integrated at the wall. Standard $k$–$\omega$ SST model combines near-wall accuracy and ability to resolve the far-stream but has shown convergence difficulties in this study. Therefore, standard $k$–$\varepsilon$ is chosen as the turbulence model. To improve near-wall treatment, standard wall function in FLUENT software (default option) is used. The wall function is known to be effective and robust for $30 < y^+ < 300$,

**Table 4**
Final $k_s$ values used in the computational models.

| Case | Initial $h$ in experiment (m) | Final $k_s$ (m) |
|---|---|---|
| **SPC (Airfoil)** | $5.28\times10^{-8}$ | $2.7\times10^{-5}$ |
| **Foul Release (Airfoil)** | $1.38\times10^{-8}$ | $1.03\times10^{-4}$ |
| **SPC (DREA)** | $5.28\times10^{-8}$ | $2.7\times10^{-4}$ |
| **Foul Release (DREA)** | $1.38\times10^{-8}$ | $1.03\times10^{-3}$ |

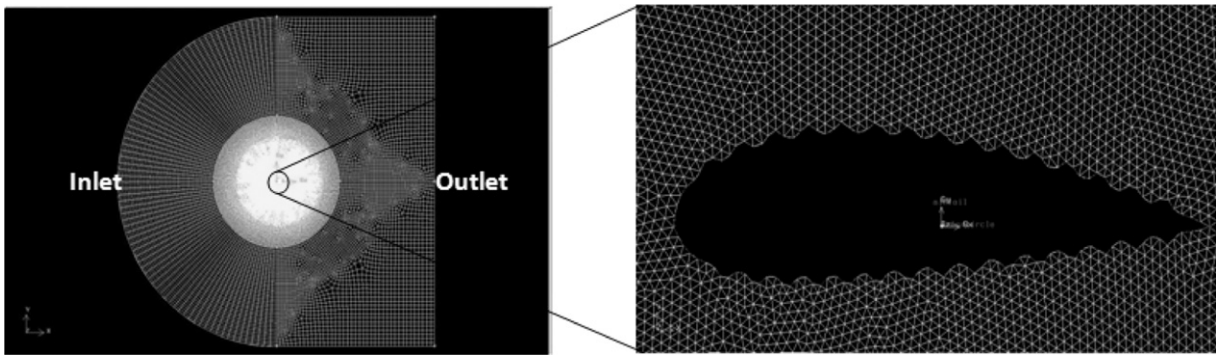


**Fig. 4.** Mesh for NACA 4424 airfoil.

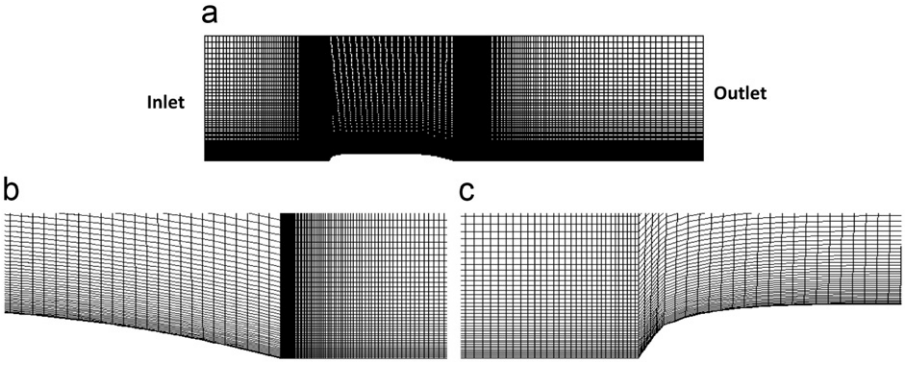


**Fig. 5.** Mesh for DREA submarine hull with detailed nose and tail meshes: (a) whole; (b) tail and (c) nose.

which matches the $y^+$ for the airfoil case. Another option for wall function, i.e. near-wall treatment proves to be ineffective in this situation as the results are not satisfactory compared to experimental results. This is probably due to the high $y^+$ value for the airfoil case. However, a more complex turbulence model which is adjusted for roughness effects can be set as an area for further study to improve on the set of results, particularly in cases of high fouling.

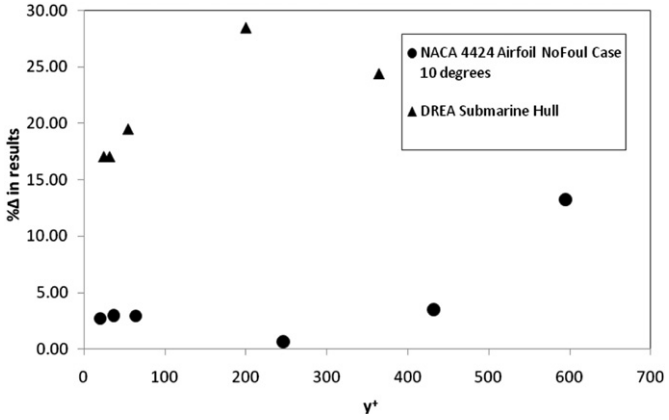


**Fig. 6.** Results at different $y^+$ values.

The transport equations for standard $k$–$\varepsilon$ model (Launder and Spalding, 1972) are:

$$\frac{\partial}{\partial t}(\rho k)+\frac{\partial}{\partial x_i}(\rho k u_i)=\frac{\partial}{\partial x_j}\left[\left(\mu+\frac{\mu_t}{\sigma_k}\right)\frac{\partial k}{\partial x_j}\right]+P_k+P_b-\rho\epsilon-Y_M+S_k \quad (10)$$

$$\frac{\partial}{\partial t}(\rho\epsilon)+\frac{\partial}{\partial x_i}(\rho\epsilon u_i)=\frac{\partial}{\partial x_j}\left[\left(\mu+\frac{\mu_t}{\sigma_\epsilon}\right)\frac{\partial\epsilon}{\partial x_j}\right]+C_{1\epsilon}\frac{\epsilon}{k}(P_k+C_{3\epsilon}P_b)-C_{2\epsilon}\rho\frac{\epsilon^2}{k}+S_\epsilon \quad (11)$$

$$\mu_t=\rho C_\mu\frac{k^2}{\epsilon} \quad (12)$$

Eqs. (10) and (11) are for the turbulent kinetic energy $k$ and turbulence dissipation $\varepsilon$, respectively, and Eq. (12) is the calculation of turbulent viscosity $\mu_t$. $P_k$ represents the generation of $k$ due

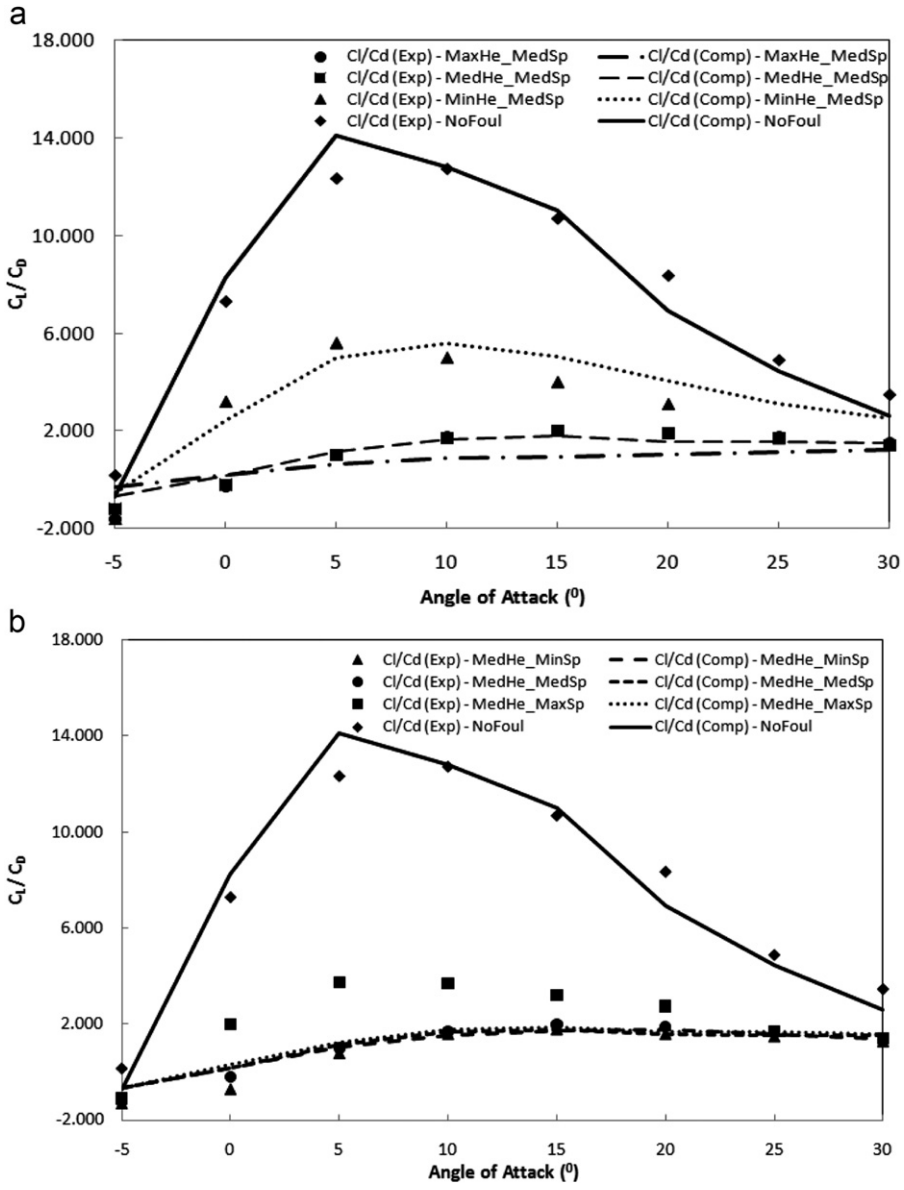


**Fig. 7.** Lift/drag results for NACA 4424 airfoil at different angles of attack: (a) results based on fouling height and (b) results based on fouling density.

to mean velocity gradients and $P_b$ represents generation of $k$ due to buoyancy. $Y_M$ represents the contribution of fluctuating dilatation in compressible turbulence to overall dissipation rate. $C_{1\varepsilon}$, $C_{2\varepsilon}$ and $C_{3\varepsilon}$ are constants. $\sigma_k$ and $\sigma_\varepsilon$ are the turbulent Prandtl numbers for $k$ and $\varepsilon$, respectively. $S_k$ and $S_\varepsilon$ are source terms.

### 2.3.2. Grid and meshing

In turbulent and viscous flows, it is important to resolve the wake beyond the trailing edge. For this reason, C-grid is used for the airfoil as high resolution can be concentrated at the trailing edge. Typically, a C-grid will consist of a semi-circle face followed by 2 square or rectangular faces. An airfoil is usually tested at a range of different angles of attack so different C-grid has to be created for each angle of attack. This is done instead of changing the angle of the flow so that the high resolution near the trailing edge can be preserved. The radius of the inner circle is 10$c$ and the radius of the outer circle is 25$c$. The radius of the outer circle is equal to the length of the side of each individual square beyond the trailing edge. The term $c$ refers to the chord length, which in this case is 0.2 m. Near-wall grid is arranged clustering to the wall to accurately capture the force and boundary layer flow field. Unstructured grid is used in the inner circle because of the 'spikes' on the airfoil. The detailed mesh distribution for NACA 4424 is displayed in Fig. 4.

To model DREA Submarine Hull, H-grid is used as the entire computational domain can be divided into 3 parts—the upstream, the body and the downstream as seen in Fig. 5. As spikes are not required for the submarine hull, structured grid will be used in all three domains to minimise computational time. Size of far field has to be sufficiently large to capture the entire flow. The total length of the computational domain is 4$l$, where $l$ is the total length of submarine. The upstream and downstream length is 1$l$ and 2$l$, respectively. Height of the computational domain is 1$l$ above the centreline of the body. Grid points are concentrated near the body of the hull by means of successive ratio to increase accuracy.

### 2.3.3. Numerical scheme

For convective terms such as momentum and turbulent kinetic energy, second order upwind discretisation scheme is used to ensure a higher level of accuracy for both the NACA airfoil and DREA hull. Green–Gauss node-based gradient option is chosen instead of the default Green–Gauss cell-based option because the former is more useful for hybrid meshes. As the DREA hull case contains only structural mesh, cell-based option is used. The SIMPLE scheme is adopted for airfoil case because no special corrections are required for pressure–velocity coupling. However, skewed elements appear in the DREA hull model, so PISO scheme is adopted instead.

### 2.3.4. Boundary conditions

For both models, velocity inlet is specified as the inlet boundary type and outflow is specified as the outlet boundary type. For the NACA airfoil model, interface boundary type is used for the two overlapping circles in the middle of the domain. For the DREA hull model, axis boundary type is used along the symmetrical line to mark symmetry of the case. In the antifouling case, the wall boundary type for the airfoil and DREA body was

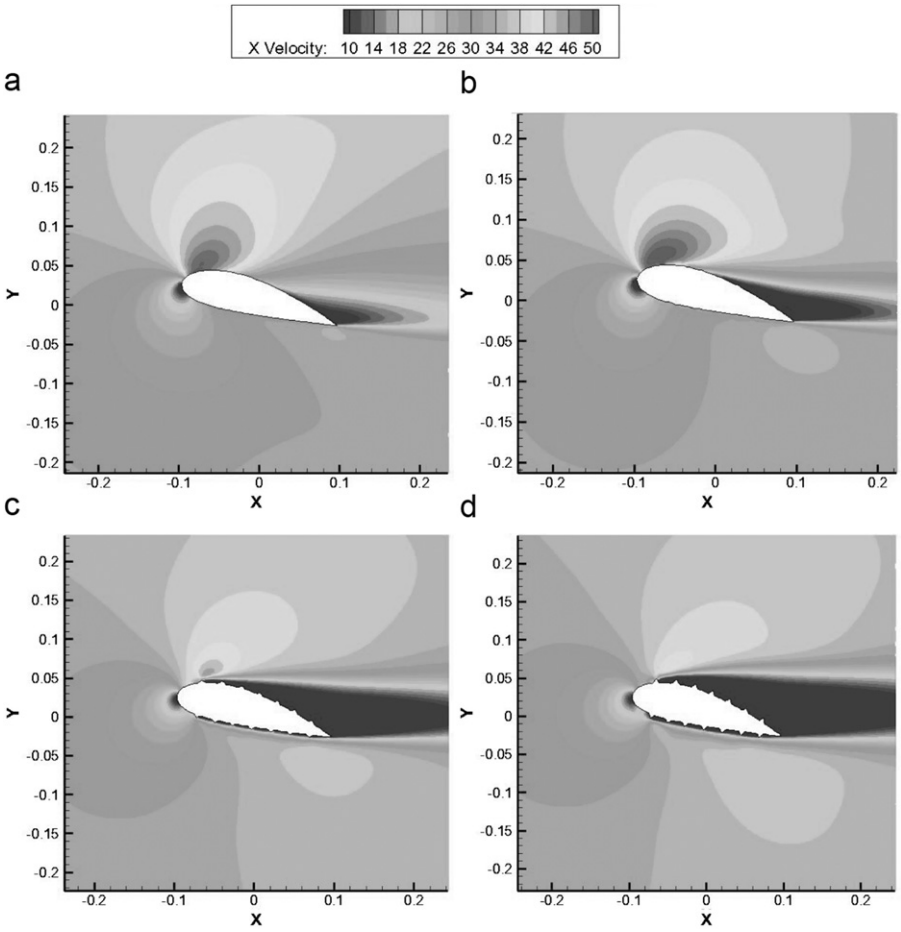


**Fig. 8.** $x$-Velocity contour plots at $\alpha = 15^\circ$ for NACA 4424 airfoil at different fouling heights: (a) NoFoul; (b) MinHe_MedSp; (c) MedHe_MedSp and (d) MaxHe_MedSp.

modified to include roughness effects caused by the antifouling. For the velocity inlet, turbulence intensity and turbulent length scale have to be provided. As full data from experiment was not available, estimated values were used.

#### 2.3.5. Hydrodynamic parameters

Lift is the component of the aerodynamic force perpendicular to the direction of motion. Change in lift is explained by the Bernoulli effect. When fluid is moving at a greater velocity, pressure exerted on it is lower and when fluid is moving at a lower velocity, pressure exerted on it is higher. This difference in pressure between upper and lower surfaces gives rise to lift.

Lift force can be obtained through experimental model testing or computational method such as CFD. Lift coefficient $C_L$ is usually preferred as a non-dimensional parameter for lift, $L$:

$$C_L = \frac{L}{(1/2)\rho U^2 A} \tag{13}$$

Drag is the component of aerodynamic force opposite to the direction of motion. Drag is usually countered by thrust which is provided by a propelling mechanism which can be air, engine-powered propeller or others. Drag does depend on velocity as outlined in the equation similar to the lift equation:

$$C_D = \frac{D}{(1/2)\rho U^2 A} \tag{14}$$

The wall surface pressure coefficient $C_p$ is defined as

$$C_p = \frac{p - p_{ref}}{q_{ref}} \tag{15}$$

where $p$ is the static pressure, $p_{ref}$ is the reference pressure and $q_{ref}$ is reference dynamic pressure as defined in following equation:

$$q_{ref} = \frac{1}{2}\rho_{ref} v_{ref}^2 \tag{16}$$

## 3. Results and discussions

### 3.1. Grid dependence test

It is generally acceptable that the mean distance of the first grid point from the wall ($y_p$) has to be sufficiently small for the turbulence to be captured. This distance is characterised by $y^+$ value. Here $y^+$ is defined as $y^+ = (\rho y_p u_\tau)/\mu$ where $u_\tau$ is turbulence friction velocity, qualified by $u_\tau = (\tau_w/\rho)^{1/2}$ with $\tau_w$ being the wall shear stress. Although FLUENT recommends that $y^+$ value should be within 30–300 for most turbulence models, the minimum $y^+$ value differ for each case. Reducing the $y^+$ value below this point through grid adaption will not produce significant change in results. The results are therefore grid independent. Our tests are carried out for NACA 4424 airfoil Nofoul case at angle of attack of 10° and DREA submarine hull. The first case is chosen because value of $C_L/C_D$ is high so changes are more

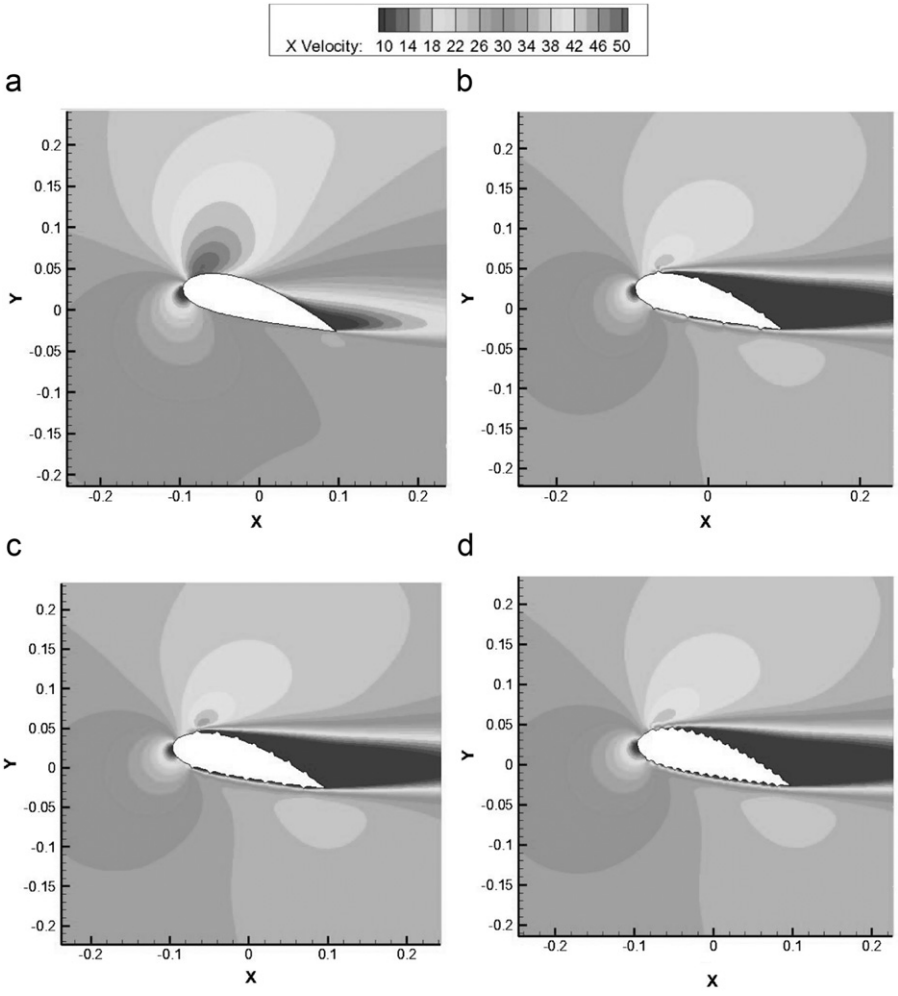


**Fig. 9.** $x$-Velocity contour plots at $\alpha = 15°$ for NACA 4424 airfoil at different fouling densities: (a) NoFoul; (b) MedHe_MaxSp; (c) MedHe_MedSp and (d) MedHe_MinSp.

visible. Fig. 6 shows the change of $C_L/C_D$ with the variation of $y^+$ for two cases. As seen, for NACA 4424 airfoil, no significant change is observed after $y^+$ reduced to 100. For DREA hull, results stop changing after $y^+=31.18$. The significant influence of $y^+$ value on the results of DREA hull is logical as the wall (surface of the hull) is relatively smooth so near-wall grid density is important to capture the turbulence. With such a high maximum $y^+$ value for airfoil cases, standard wall equation is employed for all cases with standard $k$–$\varepsilon$ equation.

### 3.2. NACA 4424 results

In this section, we discuss the computational results for NACA 4424 foil case with fouling and antifouling effect.

#### 3.2.1. Lift and drag

The variation of $C_L/C_D$ with angle of attack are shown in Fig. 7 for different fouling levels and compared with experimental results from Orme et al. (2001).

As seen clearly, our results are in good agreement with experiments for either fouling density based or fouling height based. The values of $C_L/C_D$ differ significantly at varying fouling heights but that is not obvious at varying fouling densities. Also, the excellent agreement with experiments are obtained at lower fouling cases. As indicated, for NoFoul case and low fouling height (MinHe_MedSp), the stall points are well captured. With increase of fouling height, stall occurs at higher values of angle of attack (AOA). It is also noted that the $C_L/C_D$ exponentially decreases with fouling on the foil surface and the extent of decrease decays with fouling density and height.

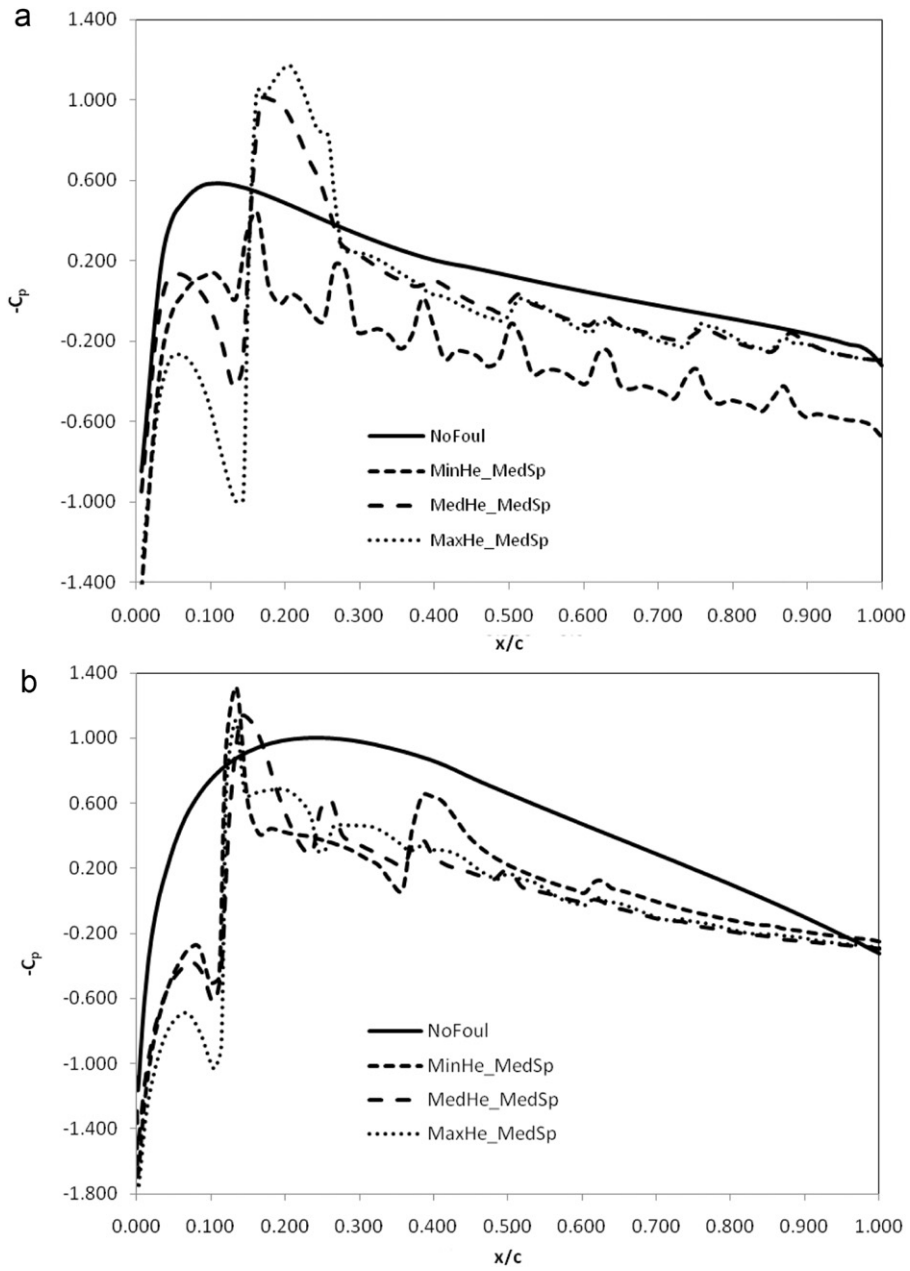


**Fig. 10.** Wall pressure coefficient distribution at $\alpha=15^\circ$ for NACA 4424 airfoil based on fouling height: (a) upper surface and (b) lower surface.

### 3.2.2. Velocity contours

The streamwise velocity ($x$-velocity) contour for various fouling height and fouling spacing are shown in Figs. 8 and 9, respectively, at AOA of 15°. It is well known that the flow seperation has a strong impact on the lift and drag performance. As seen from these figures, the extent of flow separation at trailing edge is revealed clearly here. At lower fouling cases, favourable pressure gradients (regions of high velocity) are more significant. At higher fouling cases, separation happens earlier and favourable pressure gradient is much smaller resulting in lower lift. In other words, flow is stalled in the worse fouling case.

### 3.2.3. Surface pressure distribution

The foil surface pressure distributions at AOA of 15°, represented by pressure coefficient defined in Eq. (15), are shown in Figs. 10 and 11 for fouling height and density, respectively.

From Fig. 10, it can be observed that the general trend of $C_p$ variation along chord length is the same for fouling and NoFoul. However, pressure gradient gradually became adverse as height of fouling increases. Stagnation point occurs at about 0.1–0.22 chord length from the leading edge. At higher fouling cases, stagnation point moves closer to the leading edge. Spikes are clearly seen from fouling curves which is caused by the geometric spikes modelling the various fouling heights. The increased peak values of $C_p$, corresponding to the stall, is present with increasing of fouling height. The steep change for fouling cases around $x/c=0.1$ is consistent with the peak pressure value for the NoFoul case, indicating a low velocity region or separation point as shown in $x$-velocity contour plots in Figs. 8 and 9. With increase in fouling height, the velocity in this region becomes significantly lower than its neighbouring areas causing steeper variation of surface pressure.

Pressure distribution remains largely the same for different fouling densities but there are more fluctuations in the pressure for the densest fouling case as revealed in Fig. 11. This is natural as the high number of spikes causes frequent pressure changes in the flow. Similarly, the stagnation point moves closer to the leading edge at denser fouling cases.

### 3.2.4. Turbulent kinematic energy

The turbulent kinetic energy $k=(1/2)(\overline{u'^2}+\overline{v'^2}+\overline{w'^2})$ contours for NACA 4424 airfoil at $\alpha=15°$ are plotted in Figs. 12 and 13 for different fouling heights and density, respectively. The turbulent kinematic energy ($k$) increases with fouling height as clearly seen from plot near the foil top surface and extends into wake due to

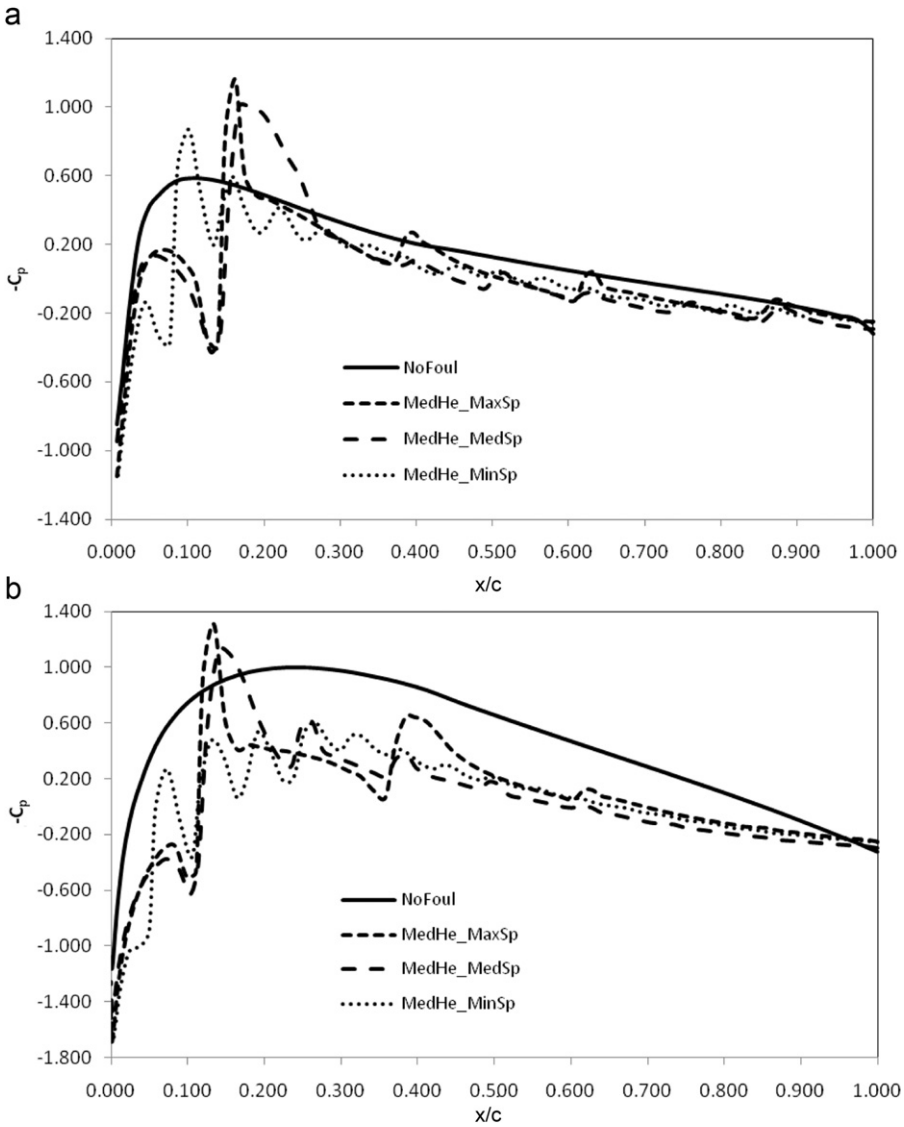


**Fig. 11.** Wall pressure coefficient distribution at $\alpha=15°$ for NACA 4424 airfoil based on fouling density: (a) upper surface and (b) lower surface.

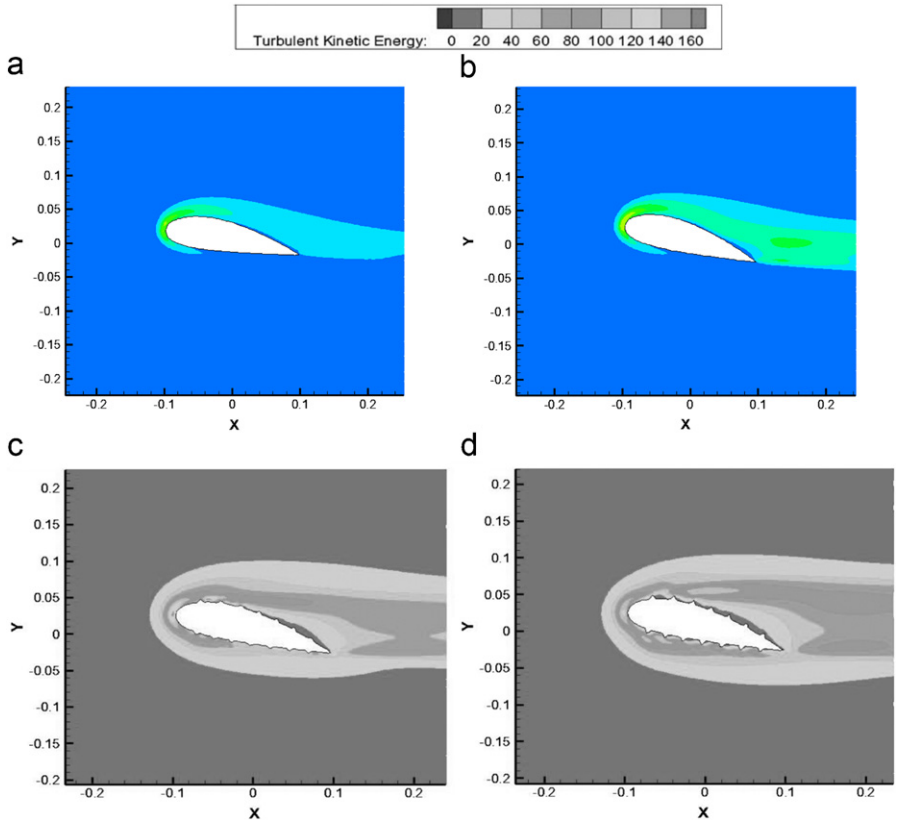


**Fig. 12.** Turbulent kinetic energy contours at $\alpha=15^{\circ}$ for NACA 4424 airfoil at different fouling heights: (a) NoFoul; (b) MinHe_MedSp; (c) MedHe_MedSp and (d) MaxHe_MedSp.

the flow separation. Local highest intensity $k$ at the leading edge is observed which is more apparent at MedHe_MedSp case.

#### 3.2.5. Antifouling effect

The antifouling effect with two different methods on the $C_L/C_D$ versus angle of attack is shown in Fig. 14 along with NoFoul results. The Foul Release results are very close to NoFoul case indicating that fouling effect is efficiently removed with the imposed Foul Release materials. For SPC, the effect of improving lift performance is not so good compared to Foul Release, especially at the region near the stall appearing. This behaviour is related to the flow field as shown in Fig. 15 for velocity contours with fouling, SPC antifouling and Fouling Release.

### 3.3. Results for submarine

#### 3.3.1. Bare hull

For validation, a modelling of bare DREA submarine hull was conducted and the computed drag coefficient is compared with other available experimental and simulation results are summarised in Table 5. As seen, our result shows close agreement with the experimental data and in comparison with other data obtained via computational effort. Therefore, approach is validated and the computational model of DREA submarine will be used for antifouling simulations.

Figs. 16 and 17 show the static pressure and $x$-velocity contours of the DREA hull, respectively. A high pressure point (stagnation) is shown at the nose of hull followed by a low pressure region in the front section. At the rear part of hull near the tail, a relative high pressure is achieved. Corresponding velocity contour plotted in Fig. 17 show the reversed high/low velocity regions related to the pressure fields.

#### 3.3.2. Antifouling results

Antifouling is quantified with hull drag coefficient $C_D$. The computed $C_D$ with two antifouling methods, i.e. SPC and Foul Release are compared with NoFoul case in Table 6. Similar to NACA 4424 airfoil, Foul Release antifouling obtained the closer $C_D$ as NoFoul case with the relative low drag coefficient.

The turbulent kinetic energy contours are shown in Fig. 18 for near nose part of DREA hull. As we can see, turbulent kinetic energy peaks inside the thin boundary layer surrounding the surface. Away from surface, the level of $k$ is observed to drop. Apparent difference in turbulence kinetic energy is not shown from $k$ plot among three test cases. However, the surface turbulence kinetic energy variation with streamwise length is displayed in Fig. 19. Clearly seen, highest turbulence occurs near the leading edge but the presence of antifouling has pushed the maximum point slightly away from the leading edge. It is also observed that turbulence caused by SPC is significantly higher as compared to Foul Release.

The pressure coefficient distribution is shown in Fig. 20. Similar to NACA foil case, results for Foul Release is closer to NoFoul case. Local peak value of pressure near the leading edge corresponds to the maximum turbulent kinetic energy shown in Fig. 19.

### 3.4. Relevance to marine engineering

Drag coefficient, $C_D$, is a non-dimensionalised value of the drag force, $D$. Drag force contributes to resistance experienced by a body. Total resistance, $R_t$ has a direct relationship with

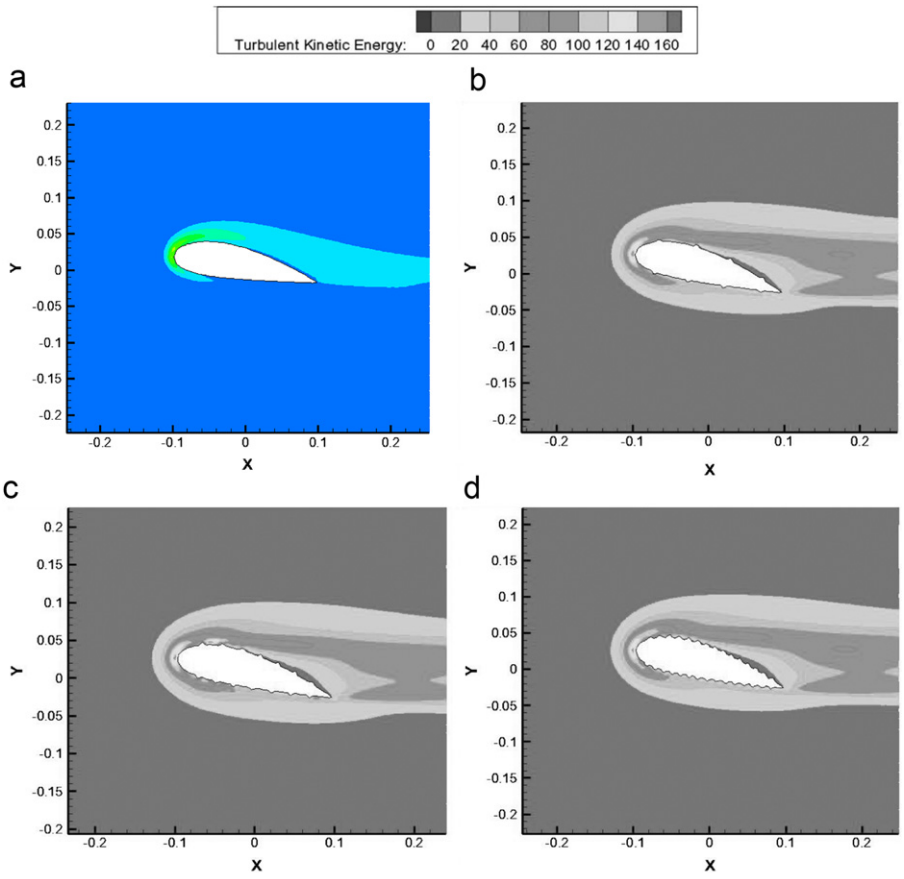


**Fig. 13.** Turbulent kinetic energy contours at $\alpha=15^{\circ}$ for NACA 4424 airfoil at different fouling densities: (a) NoFoul; (b) MedHe_MaxSp; (c) MedHe_MedSp and (d) MedHe_MinSp.

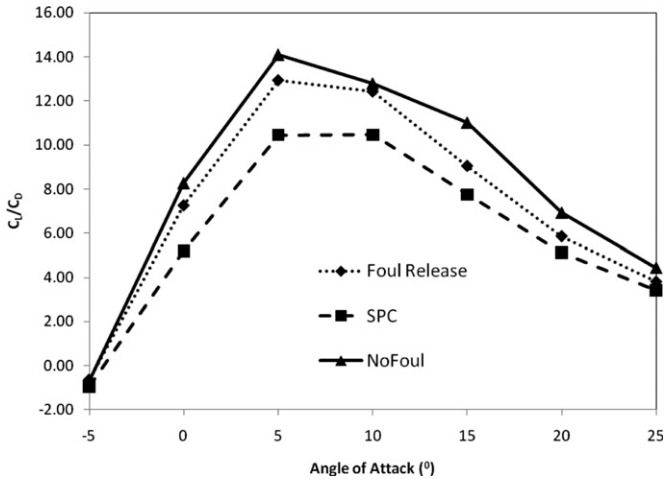


**Fig. 14.** Comparison of $C_L/C_D$ for different antifouling methods.

effective power, $P_e$:

$$P_e = R_t V_s \quad \text{(kW)} \tag{17}$$

If ship service speed $V_s$ remains unchanged, ship will require higher effective power $P_e$ from the propeller and brake power $P_b$ from the main engine as resistance $R_t$ increases. Brake power also has a direct relationship with mass of fuel consumed, $m_f$:

$$P_b = \frac{m_f}{SFC\ Endurance} \quad \text{(kW)} \tag{18}$$

Specific fuel oil consumption (SFC) depends on the engine efficiency and endurance depends on the specific journeys. Therefore, they can be assumed to be constant to compare $P_b$ and $m_f$ in the case of fouling. From the series of equations, there is a link between fouling and fuel consumption.

American Bureau of Shipping (ABS) has set in its rules 7-3-2/5.1 that a special survey which includes dry-docking has to be carried out every 3 or 5 years. Most other classification societies set the same requirements. Although Foul Release is more expensive, it exhibits lesser surface drag due to roughness (11.4–30%) and in the long run, this can lead to cost savings. Furthermore, present simulation was done on a small airfoil of length 0.2 m so the fuel savings effect will be more significant for a large vessel.

Industrial estimates from reference 9 show that it costs roughly £60 per square metre for application of Foul Release, regardless of the dry-docking interval. It costs £40.50 per square metre for application of SPC for 3-year dry-docking interval and £51 per square metre for 5-year interval. All these values are inclusive of blasting, washing and paint application by airless spray. Based on a standard vessel with a typical surface area of about 10,700 $m^2$, an additional £210,000 is required for Foul Release for 3-year dry-docking interval and additional £96,500 is required for 5-year dry-docking interval as compared to SPC. However, the increased drag in SPC will result in an increase in fuel oil consumption. It is believed that the cost advantage of SPC can be easily offset by its increased drag due to roughness. Therefore, based on these factors, Foul Release is almost certainly the better option for 5-year dry-docking interval with high ship activity.

Such simple comparison has to be made on neglected factors which will influence the pricing. Firstly, price will depend on

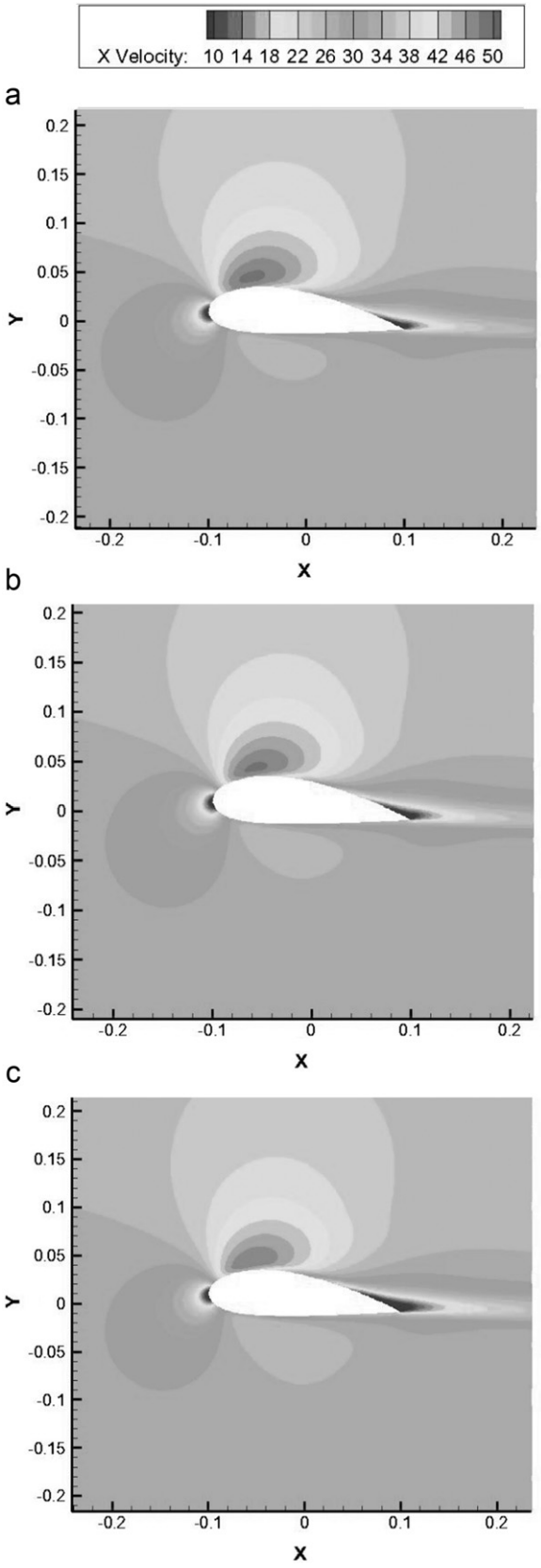


**Fig. 15.** Different antifouling effect on $x$-velocity contours for NACA 4424 airfoil at $\alpha=5^{\circ}$: (a) NoFoul; (b) Foul Release and (c) SPC.

whether it is the first-time application or a re-coat. Next, paint thickness also matters and it will depend on the individual vessel's activity. However, these factors are not relevant for this

**Table 5**
Drag coefficient of DREA submarine hull obtained by different methods.

| $C_D$ (Present comp.) | $C_D$ (exp.) | $C_D$ (Baker, 2004) | $C_D$ (Karim et al., 2009) | Difference with experimental data (%) |
|---|---|---|---|---|
| 0.00144 | 0.00123 | 0.00167 | 0.00104 | 17.07 |

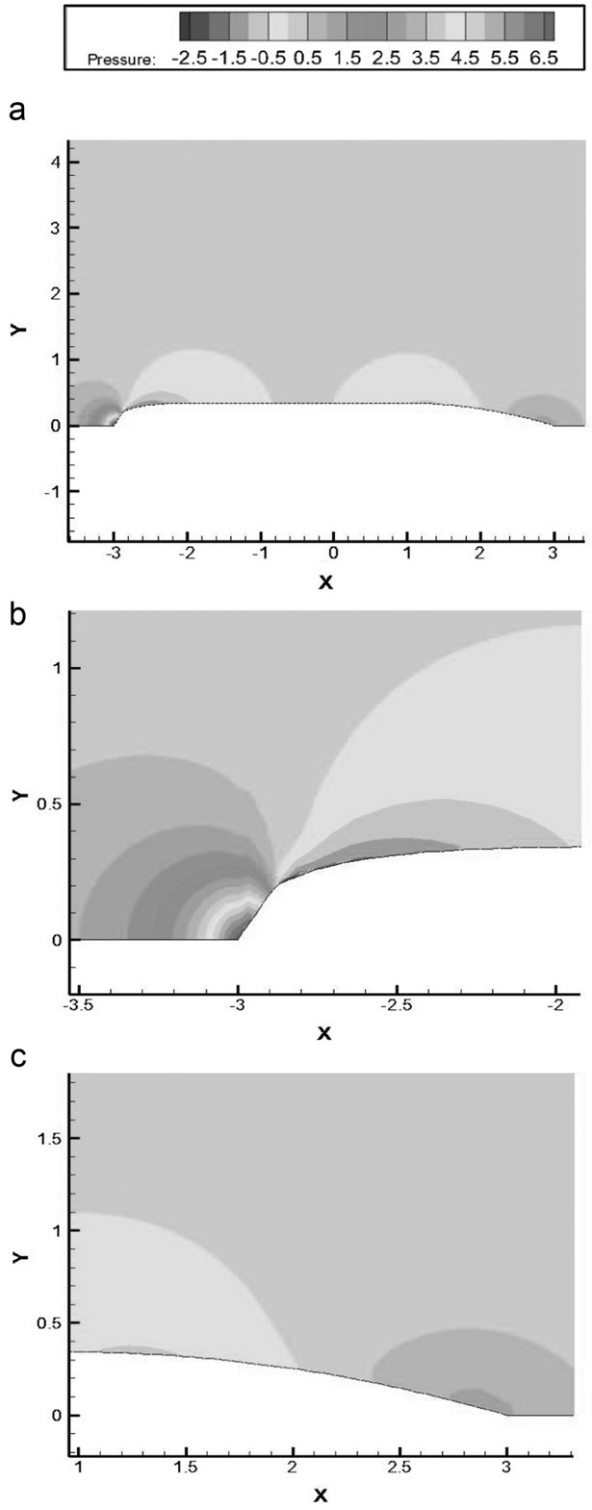


**Fig. 16.** DREA submarine pressure contours: (a) whole; (b) nose and (c) tail.

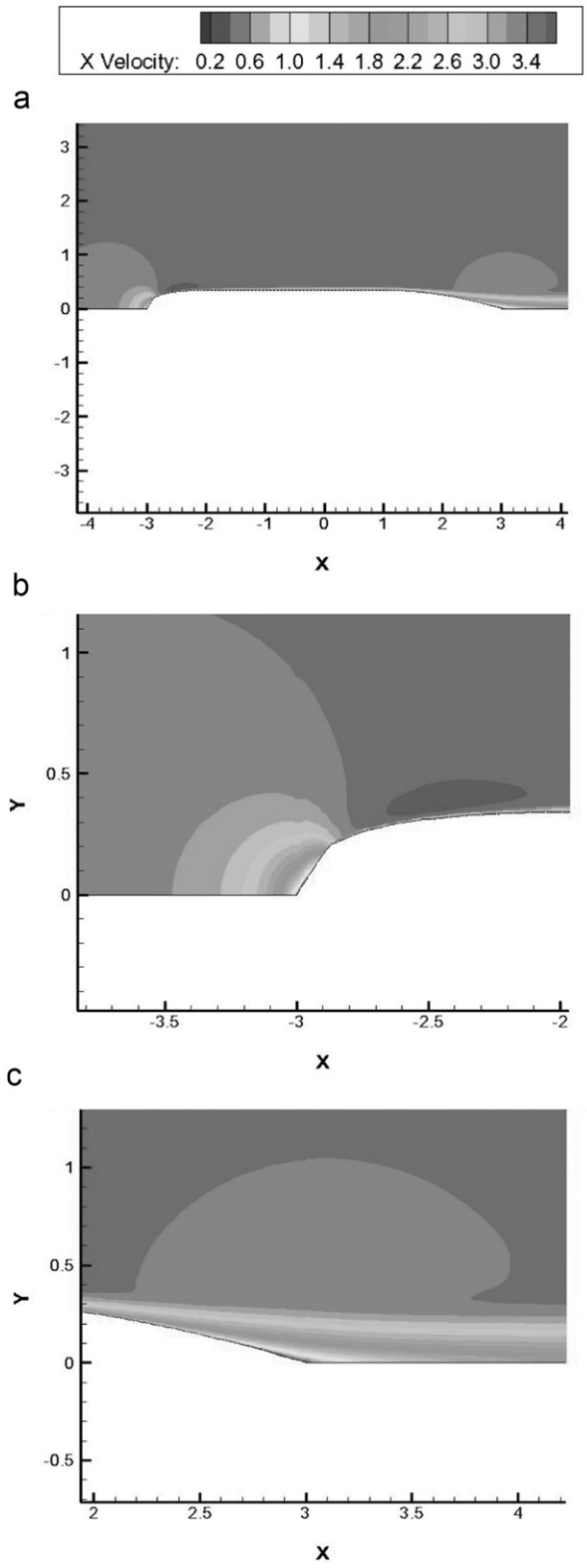


**Fig. 17.** *x*-Velocity contours for DREA hull: (a) whole; (b) nose and (c) tail.

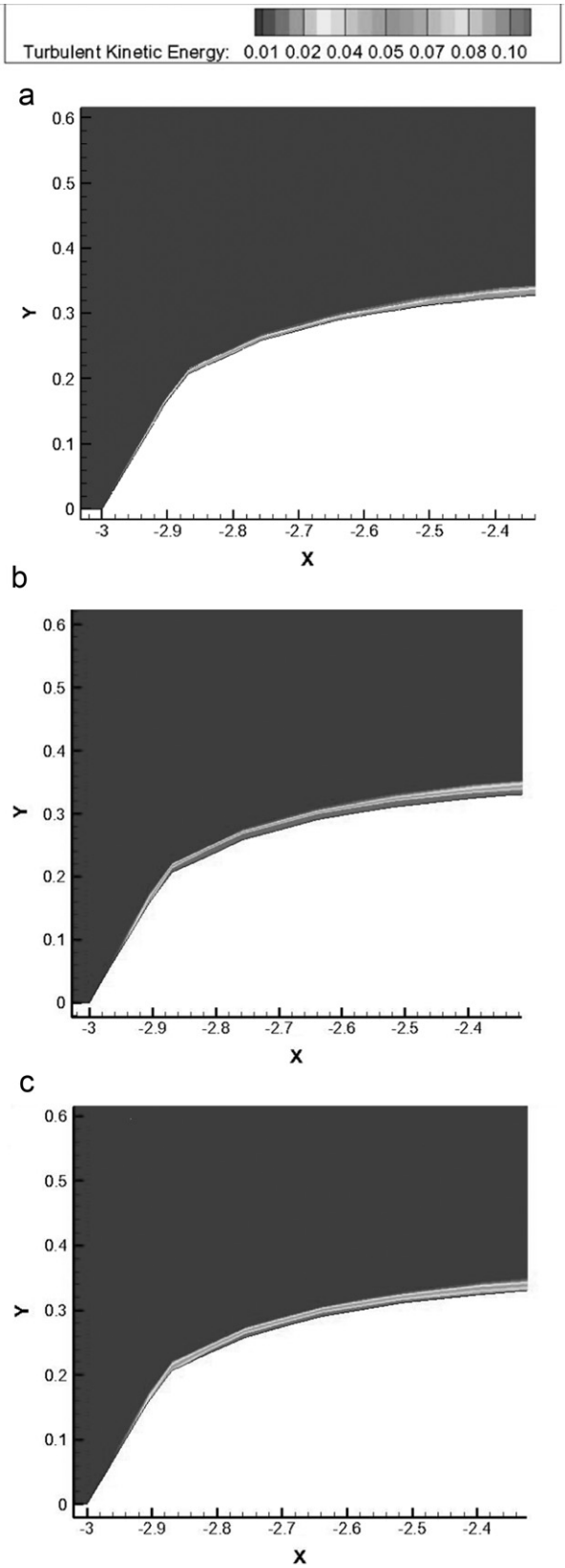


**Fig. 18.** Turbulent kinetic energy plots for nose of DREA submarine hull: (a) NoFoul; (b) Foul Release and (c) SPC.

**Table 6**
Drag coefficient of DREA submarine hull for different antifoulings.

| NoFoul | Foul Release (FR) | SPC | Difference between FR and SPC (%) |
|---|---|---|---|
| $C_D$ | | | |
| 0.00144 | 0.00148 | 0.00174 | 17.57 |

research. Nevertheless, this illustrates an area where the data produced in this project can be used.

A common criticism of CFD papers is the lack of applicability in the real marine industry. This paper combines CFD with a very

practical long-lasting problem in the marine industry: fouling. The effects of fouling on flow around a body were explained by the contours and plots of outputs from FLUENT software. The contours and plots consolidate the lift and drag values and provide a useful insight into the causes of the changes in lift and drag.

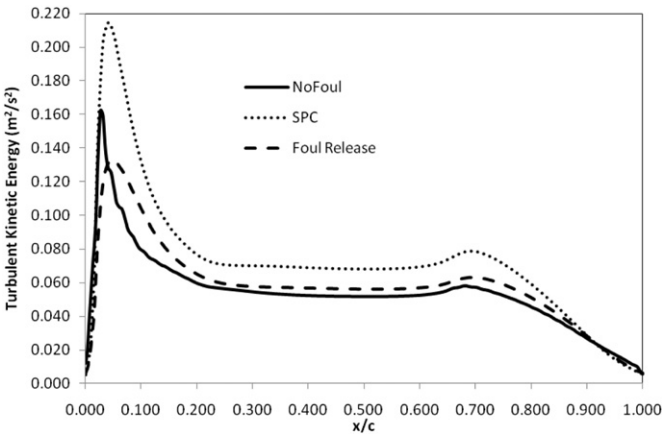


**Fig. 19.** Turbulent kinetic energy distribution for DREA.

However, there are a few limitations to consider in this simulation. Firstly, simulation was done in two-dimensional instead of three-dimensional. The simulation was therefore much quicker to complete and the complexity was reduced but there was compromise in terms of accuracy of results. Secondly, the roughness caused by antifouling paints is usually non-uniform. However, it will involve necessarily much more effort in FLUENT software so uniform roughness was being used. The difference in results was not expected to be significant as long as the physics is concerned.

## 4. Conclusion

It has been shown in this paper that CFD can be used to model fouling effects and standard $k$–$\varepsilon$ model with standard wall equation produces generally acceptable results.

Fouling on NACA 4424 airfoil reduces lift–drag ratio by up to 80%, especially at low angles of attack and will therefore contribute significantly to increase in fuel consumption. Detailed examination on the flow structure, including the velocity contour, surface pressure distribution and turbulence kinetic energy distribution, shows that fouling shifts the stagnation point towards

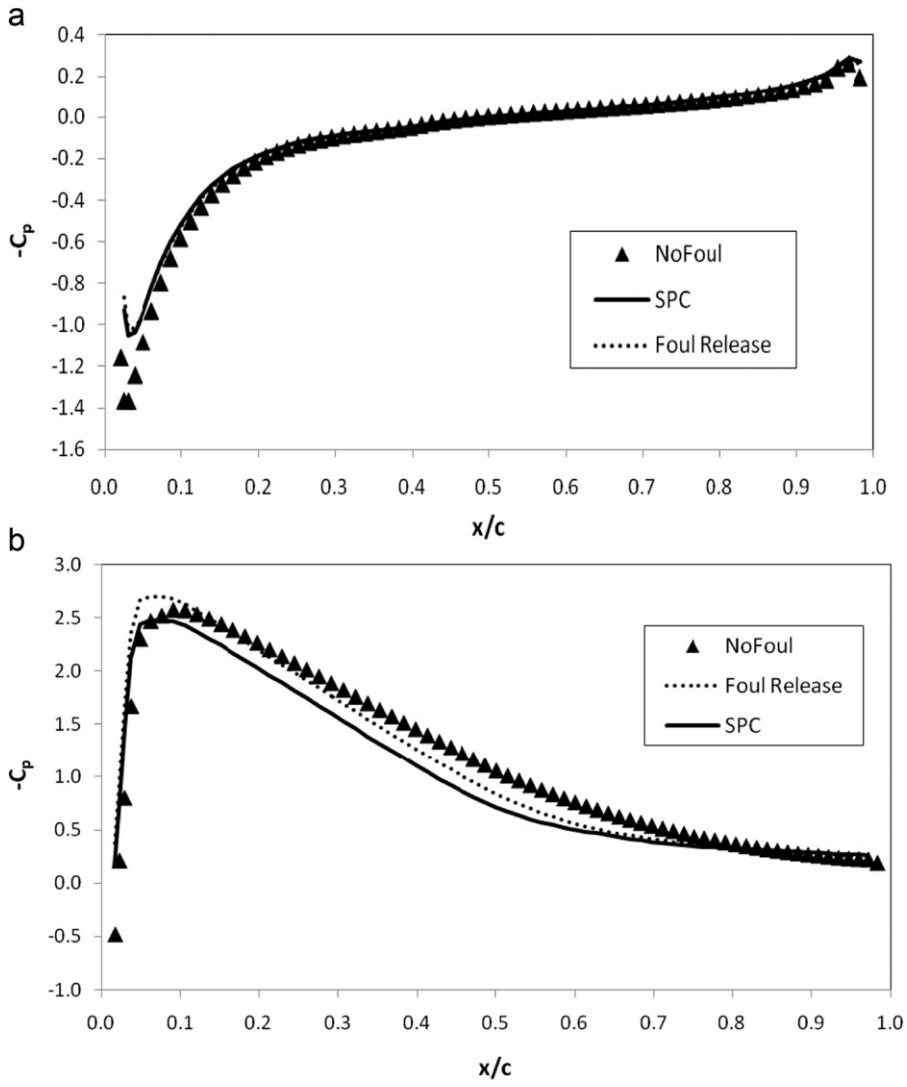


**Fig. 20.** Pressure coefficient plots for DREA submarine hull with different antifoulings: (a) upper portion of DREA submarine hull and (b) lower portion of DREA submarine hull.

the leading edge and creates a significant amount of separation near the trailing edge. Favourable pressure gradient is also greatly reduced by fouling which has led to lower lift.

Antifouling, despite its main function to prevent biofouling, promotes roughness and has lead to up to 40% increase in $C_L/C_D$. However, Self Polishing Copolymer (SPC) exhibits higher turbulence near boundary layer and lower $C_L/C_D$ as compared to Foul Release. This higher turbulence causes a reduction of $C_L/C_D$ from 18% to 37%. For the DREA case, the $C_D$ is shown to increase by up to 20% when antifouling is applied. This increase in $C_L/C_D$ is associated with the increase in turbulence near the boundary layer for the DREA case. Despite the lower cost of its applications on ship hulls, the extra drag exhibited by SPC is likely to offset that advantage as compared to Foul Release, depending on the ship's activity. Many large tankers and bulkers should find cost effectiveness with Foul Release.

Although some limitations exist in the present modelling, such as those resulting from two-dimensional and uniform roughness assumption, the results presented here can prove to be useful for industrial firms from both sides of the antifouling trade—ship operators and paint companies. Furthermore, flow around a fouled surface is a novel concept and will be of interest to fluid dynamic academia.

## Acknowledgements

The authors would like to thank Dr. Ian Masters in Swansea University for providing the experimental data and to Dr. Colin Anderson in International Paint Ltd., UK, who provided information for estimation of antifouling economic cost.

## References

Anderson, J.D., 1995. Computational Fluid Dynamics: The Basics with Applications, 1st edition McGraw-Hill International Editions.

Anderson, C., 2006. Newcastle University Lecture 2: Antifouling. [Internet] Newcastle University. Available at: 〈http://research.ncl.ac.uk/cavitation/archive/NclUni_Lect2_1106.pdf〉.

Baker, C., 2004. Estimating drag forces on submarine hulls. Defence Research and Development Canada.

Candries, M., Atlar, M., 2003. The measurement of the drag characteristics of tin-free self-polishing co-polymers and fouling release coatings using a rotor apparatus. Biofouling: The Journal of Bioadhesion and Biofilm Research, 1029-2454 19 (1), 27–36 Suppl. 1.

Drake, J.M., Lodge, D.M., 2007. Hull fouling is a risk factor for intercontinental species exchange in aquatic ecosystems. Aquatic Invasions 2 (2), 121–131.

Epstein, N., 1981. Fouling: Technical Aspects, in Fouling of Heat Transfer Equipment. In: Somerscales, E.F.C., Knudsen, J.G. (Eds.), Hemisphere, Washington, DC, pp. 31–53.

Ghobashy, A.F.A., El Komy, M.M., 1980. Fouling in Lake Timsah (Egypt). Netherlands Journal of Aquatic Ecology 14 (3), 169–178.

Hentschel, E., 1923. Der Bewuchs an Seeschiffen (The fouling of ships). International Review of Hydrobiology, 238–264.

ITTC, 2005. ITTC—recommended procedures and guidelines: testing and extrapolation methods, propulsion, performance, predicting powering margins. ITTC.

Karim, M.M., Rahman, M.M., Alim, M.A., 2009. Computation of axisymmetric turbulent viscous flow around sphere. Journal of Scientific Research 1 (2), 209–219.

Launder, B.E., Spalding, D.B., 1972. Lectures in Mathematical Models of Turbulence. Academic Press, London, England.

Ndinisa, N.V., Fane, A.G., Wiley, D.E., Fletcher, D.F., 2006. Fouling control in a submerged flat sheet membrane system: Part II—two-phase flow characterization and CFD simulations. Separation Science and Technology 41 (7), 1411–1445.

Orme, J.A.C., Masters, I., Griffiths, R.T., 2001. Investigation of the effect of biofouling on the efficiency of marine current turbines. In: Proceedings of Marine Renewable Energy Conference (MAREC), pp. 91–99.

Rajagopal, S., Nair, K.V.K., Van Der Velde, G., Jenner, H.A., 1997. Seasonal settlement and succession of fouling communities in Kalpakkam, east coast of India. Netherlands Journal of Aquatic Ecology 30 (4), 309–325.

Townsin, R.L., Medhurst, J.S., Hamlin, N.A., Sedat, B.S., 1984. Progress in calculating the resistance of ships with homogeneous or distributed roughness. In: N.E.C.I.E.S. Centenary Conference on Marine Propulsion, Paper 6.

Visscher, J.P., 1927. Nature and extent of fouling of ships' bottoms. Bulletin of Bureau of Fisheries, 193–252.

Woods Hole Oceanographic Institute, 1952. Marine Fouling and its Prevention. George Banta Publishing Co.

Wood, E.J.F., Allen, F.E., 1958. Common marine fouling organisms of Australian waters. Department of the Navy, Navy Office, Melbourne.